nanomaterials

MDPI

Article

Engineering of $Ni(OH)_2$ Modified Two-Dimensional $ZnIn_2S_4$ Heterostructure for Boosting Hydrogen Evolution under Visible Light Illumination

Huan Wang [1,2,*], Baorui Shao [2], Yaodan Chi [1], Sa Lv [1], Chao Wang [1], Bo Li [2], Haibin Li [2], Yingui Li [2] and Xiaotian Yang [1,3,*]

1 Key Laboratory for Comprehensive Energy Saving of Cold Regions Architecture of Ministry of Education, Jilin Jianzhu University, Changchun 130118, China; chiyaodan@jlju.edu.cn (Y.C.); lvsa82@163.com (S.L.); wangchao@jlju.edu.cn (C.W.)

2 Department of Materials Science, Jilin Jianzhu University, Changchun 130118, China; br13180828503@163.com (B.S.); q11833395833@163.com (B.L.); lhb980215@163.com (H.L.); l15584271740@163.com (Y.L.)

3 Department of Chemistry, Jilin Normal University, Siping 136000, China

* Correspondence: wanghuan@jlju.edu.cn (H.W.); hanyxt@163.com (X.Y.); Tel.: +86-0431-84566327 (H.W.); +86-0434-3295002 (X.Y.)

Abstract: Developing efficient catalysts to produce clean fuel by using solar energy has long been the goal to mitigate the issue of traditional fossil fuel scarcity. In this work, we design a heterostructure photocatalyst by employing two green components, $Ni(OH)_2$ and $ZnIn_2S_4$, for efficient photocatalytic H_2 evolution under the illumination of visible light. After optimization, the obtained photocatalyst exhibits an H_2 evolution rate at 0.52 mL h^{-1} (5 mg) (i.e., 4640 μmol h^{-1} g^{-1}) under visible light illumination. Further investigations reveal that such superior activity is originated from the efficient charge separation due to the two-dimensional (2D) structure of $ZnIn_2S_4$ and existing high-quality heterojunction.

Keywords: photocatalytic hydrogen evolution; charge transfer; heterostructure

check for updates

Citation: Wang, H.; Shao, B.; Chi, Y.; Lv, S.; Wang, C.; Li, B.; Li, H.; Li, Y.; Yang, X. Engineering of $Ni(OH)_2$ Modified Two-Dimensional $ZnIn_2S_4$ Heterostructure for Boosting Hydrogen Evolution under Visible Light Illumination. *Nanomaterials* **2022**, *12*, 946. https://doi.org/10.3390/nano12060946

Academic Editors: Vincenzo Vaiano and Nikos Tagmatarchis

Received: 18 December 2021
Accepted: 8 March 2022
Published: 13 March 2022

1. Introduction

Efficient utilization of solar energy for generating benign hydrogen fuel from water has long been viewed as an ideal tactic for solving issues of energy dilemma and environmental pollution. Although dramatic progress has been achieved in related research areas [1,2], it is still challenging to obtain catalysts that could meet requirements of wide absorption range, high activity, good stability, and low cost. As of now, to boost the photocatalytic activity of the catalyst, tremendous efforts have been paid to the elaborate design of visible-light-driven photocatalysts, such as noble-metal free metals, carbides, sulfides, phosphides, and their modified compounds [3–6]. Among these studies, zinc indium sulfide ($ZnIn_2S_4$) has obtained tremendous interest owing to its merits of proper bandgap (2.3–2.7 eV), low toxicity, and cost-effectiveness [7]. However, a $ZnIn_2S_4$-derived photocatalyst usually exhibits moderate activity for hydrogen photogeneration, which is supposed to be due to its fast photogenerated carrier recombination drawback. To address this, various strategies have been employed to prolong the lifetime of carriers of $ZnIn_2S_4$ for enhancing its activity, including loading noble-metal nanocrystals, doping other elements, morphology control, and construction of a heterojunction [8,9]. For example, Li et al. prepared Pt/$ZnIn_2S_4$ composites through a hydrothermal method combined with a light-induced deposition tactic. A significant increase in the photocatalytic hydrogen evolution performance of the composite was observed as expected by using ethanolamine as an electron donor [10]. Yao et al. synthesized oxygen-doping $ZnIn_2S_4$ ultrathin nanosheets via a hydrothermal method [11]. Results showed that the obtained oxygen-doped $ZnIn_2S_4$ nanosheets exhibit much enhanced photocatalytic activity under the illumination of visible light, in which they

postulated that the increased performance is possibly attributed to the effective separation of photogenerated charge carriers on the surface of the catalyst. Similarly, Yu et al. reported a $ZnIn_2S_4$@$CuInS_2$ microflower core-shell p-n heterojunction by a hydrothermal method, which could efficiently increase the charge separation efficiency and, therefore, boost the activity of photocatalytic hydrogen production [12]. Zhu et al. employed RGO as an electron acceptor and cocatalyst to modify a $ZnIn_2S_4$ sheet, and the relevant hydrogen photogeneration performance of the prepared RGO/$ZnIn_2S_4$ nanocomposite was significantly improved [13].

In addition, previous investigations indicate that various nickel-containing species, including NiO, $Ni(OH)_2$, and Ni_3B, could act as the cocatalyst for the efficient reaction of photocatalytic hydrogen production [14–16]. Among them, the heterojunction, such as $Ni(OH)_2/TiO_2$, $Ni(OH)_2/C_3N_4$, and $Ni(OH)_2$/CdS, could obviously increase its photocatalytic activity under visible light illumination, which was supposed to be attributed to the inhibition of the recombination of photogenerated carriers [17–19]. Despite the progress, a randomly designed heterojunction structure has greatly restricted the separation efficiency of photogenerated carriers. Therefore, it is of great importance to develop an effective strategy, which could significantly mitigate the low-charge separation efficiency. To reach this goal, a tactic of forming high-quality 2D/2D heterostructures, such as $Ni_2P/ZnIn_2S_4$ and $MoS_2/ZnIn_2S_4$, is proposed, which would greatly decrease the charge migration distance, and therefore, the corresponding probability of charge recombination could be largely inhibited [20,21]. This unique structure is composed of two different materials with a 2D layered structure; usually, one is as a light absorber, while the other is as a cocatalyst. Benefitting from the elaborate structural design, it possesses the merits of short diffusion distance, large interface contact area, and rich active sites, which are postulated to efficiently promote the charge separation and transfer property at the interface of the heterojunction and therefore further improve the relevant catalytic activity. Recently, preliminary attempts were made based on this concept, where the composite comprises $Ni(OH)_2$ and $ZnIn_2S_4$; [22,23] however, a further insightful investigation is still highly needed.

In this paper, the 2D $ZnIn_2S_4$ nanoflakes modified by thin $Ni(OH)_2$ nanosheets were simply prepared by employing a two-step solvothermal method. Our results demonstrate that obtained composite exhibits enhanced the performance for hydrogen photogeneration under the illumination of visible light under optimal conditions. Further, the plausible underlying mechanism is proposed accordingly.

2. Experimental Section

2.1. Synthesis of $Ni(OH)_2$ Nanosheets

The synthesis was according to previous work [24]. Typically, 1 mmol $Ni(NO_3)_2{\cdot}6H_2O$ was added into a beaker containing 20 mL ethanol under vigorous stirring. After ~10 min, 2 mL oleylamine in 10 mL ethanol was quickly added to the above solution. The obtained homogeneous solution was stirred for further 30 min and then transferred into a 50 mL Teflon-lined autoclave. The autoclave was then kept at 180 °C for 15 h, and after that, it was cooled to room temperature. The resulting green product was collected by centrifugation and washed repeatedly with cyclohexane, deionized (DI) water, and ethanol three times. Finally, the obtained product was put in a vacuum furnace at 60 °C for 6 h for further use.

2.2. Synthesis of $ZnIn_2S_4/Ni(OH)_2$ 2D/2D Composite

Typically, a certain amount of $Ni(OH)_2$ nanosheets was dispersed into 40 mL DI water with subsequent sonicating for 10 min to form a stable suspension. Then, the suspension was transferred to 100 mL of the flask containing 10 mL glycerin and magnetically stirred for 30 min. Subsequently, 272 mg of $ZnCl_2$, 1172 mg of $InCl_3{\cdot}4H_2O$, and 602 mg of thioacetamide (TAA) were added into the above flask and stirred for further 20 min. The resulting mixture was heated at 80 °C for 2 h in an oil bath with continuous stirring. The product was subjected to the centrifugation and washing (with ethanol) step three times to remove any unreacted reagents and side products and then dried at 60 °C for 6 h for

further use. Depending on the weight content of $Ni(OH)_2$, which was evaluated by the inductively coupled plasma optical emission spectrometer (ICP-OES), the as-synthesized sample was denoted as x wt% $Ni(OH)_2/ZnIn_2S_4$, and the detailed results can be found in Table S1. Pure $ZnIn_2S_4$ was also prepared as a control with a similar procedure except without introducing $Ni(OH)_2$ nanosheets during the synthesis.

2.3. Characterization

The crystal structure of all samples was accomplished on an X-ray diffractometer (Rigaku D/Max 2550, Wilmington, MA, USA, Rigaku Co., Ltd.) with a Cu Kα radiation (λ = 0.154056 nm). The morphology, elemental composition, and energy dispersive X-ray (EDX) analysis of the as-prepared samples were characterized by FE-SEM (JSM-7610F) and TEM (Fei Tecnai G2 F20 S-TWIN). XPS spectra were recorded on an ESCALAB MKII photoelectron spectrometer with Al Ka X-ray radiation. UV–VIS diffuse reflectance spectra were determined on a Shimadzu UV-2600 spectrophotometer with $BaSO_4$ as a reference. The Brunauer–Emmett–Teller (BET) surface area of the samples was measured by a Micromeritics ASAP 2020 instrument, and before the measurements, all the samples were subjected to the heating treatment under 120 °C and vacuum condition for 6 h (note: the heating treatment did not alert the crystal structure of the samples, Figure S1). Steady-state photoluminescence (PL) spectra and time-resolved transient PL decay spectra of the samples were carried out on an FLS-1000 fluorescence spectrophotometer. For steady-state PL measurements, the excitation wavelength is set to 480 nm, while for the transient PL decay spectra, the excitation and emission wavelength are set to 450 and 550 nm, respectively. The photocurrent was evaluated using the photoelectrochemical (PEC) cell with three electrodes at several on–off irradiation cycles. Electrochemical impedance spectroscopy (EIS) experiments were tested on a potentiostat (0.2 V) in the Na_2SO_4 (0.5 M) solution, with an Ag/AgCl reference electrode. Photoelectrodes used for the relevant measurements were employed FTO (fluorine-doped tin oxide) glass sheets (1.0 × 4.0 cm)as the conductive substrate, and the details of the preparation of electrode are as follows: First, the FTO electrode was successively cleaned with DI water, ethanol, and acetone by sonication, 15 min for each step. Then, a piece of tape was employed to cover the electrode, which left the exposed area fixed at 1.0 × 1.0 cm for further sample deposition. Next, 1.0 mg of relevant sample was dispersed into 0.5 mL of ethanol and subjected to sonication for 15 min. After that, 10 μL of the corresponding solution was taken and dropped onto the electrode for further measurements after it was dried under ambient conditions. ICP-OES of the samples was measured by a Thermo Scientific iCAP 6300.

2.4. Photocatalytic Reaction Measurements and Calculation

The photocatalytic hydrogen evolution reaction was carried out in a gas-tight glass flask (50 mL). Typically, 5 mg of the photocatalyst was dispersed into 15 mL DI water containing triethanolamine (TEOA) (20 vol%) as electron donors. Before the reaction, the system was evacuated and then filled with nitrogen for 5 and 30 min, respectively, to ensure the thorough elimination of residual oxygen in the system. A 300 W xenon lamp coupled with a filter (>420 nm) was used as the light source. The amount of hydrogen evolution was sampled (200 μL) from the headspace of the flask by a gas-tight syringe (Bonaduz, Switzerland, Hamilton) and immediately detected by gas chromatography (GC-2014c, Suzhou, China, Shimadzu) at given time intervals.

3. Results and Discussion

The crystal structure of different samples was obtained from XRD measurements. As shown in Figure 1, pure $Ni(OH)_2$ exhibits the characteristic diffraction peaks at 2θ = 11.7°, 24.7°, 33.1°, 35.2°, 42.5°, and 59.3°, which are indexed to the (001), (002), (110), (111), (103), and (300) crystal planes of the hexagonal crystal structure of α-$Ni(OH)_2$ (JCPDS card no. 22-0444) [25]. Interestingly, for composite samples, only peaks of $ZnIn_2S_4$ corresponding to 21.2° (006), 27.6° (102), 30.5° (104), 47.2° (110), 52.4° (116), and 55.8° (022) for planes of a

hexagonal crystal structure (JCPDS No. 65-2023) were observed, while no peak of $Ni(OH)_2$ could be detected, which is postulated to be ascribed to the low content of $Ni(OH)_2$ existing in the samples [26].

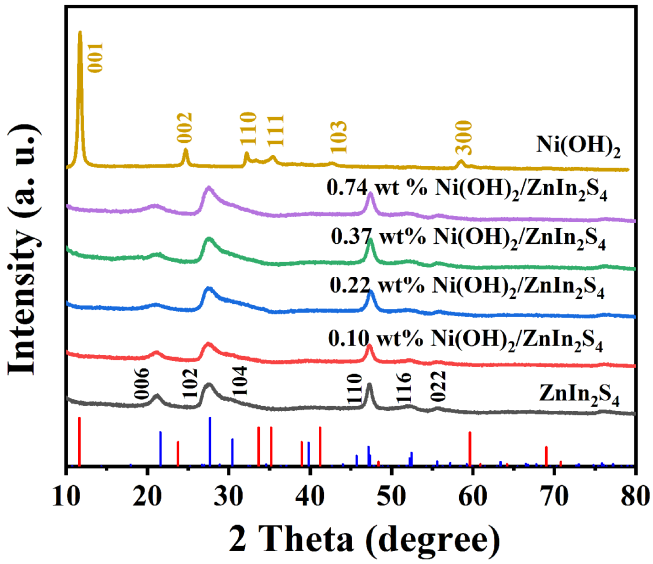

Figure 1. The XRD patterns of $ZnIn_2S_4$, $Ni(OH)_2$, and $Ni(OH)_2/ZnIn_2S_4$ composites with different contents of $Ni(OH)_2$ (0.10 wt%, 0.22 wt%, 0.37 wt%, and 0.74 wt%).

Then, the structural information of the obtained samples was acquired by SEM and TEM measurements. As an introduced material, $Ni(OH)_2$ exhibits the 2D nanoflake morphology with the in-plane size from 200 to 500 nm and the thickness at ~20 nm (Figure S2). Further coating of $ZnIn_2S_4$ As for the $Ni(OH)_2/ZnIn_2S_4$ composite, taking the 0.37 wt% one, for example, SEM image reveals that it exhibits the 2D nanoflower-like morphology with a hierarchical structure consisting of plenty of ultrathin nanosheets (Figure 2a). However, it should be noted that such morphology is well in line with that of pure $ZnIn_2S_4$, probably owing to the low introducing content of $Ni(OH)_2$.

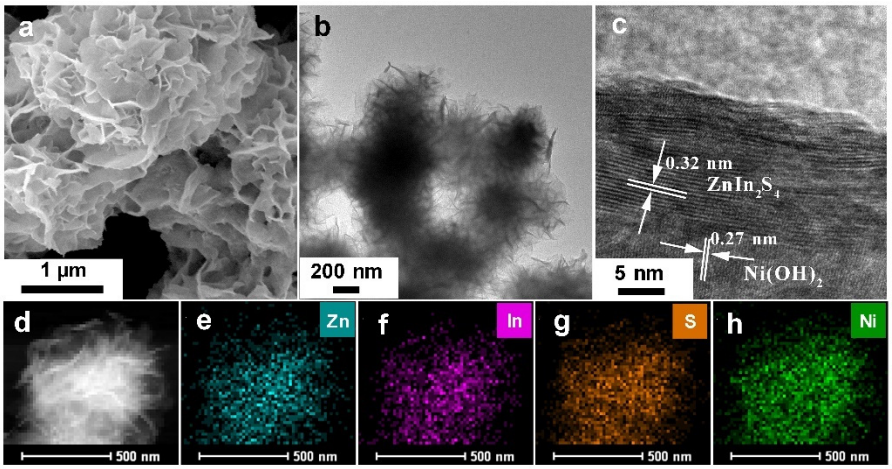

Figure 2. SEM image (**a**), TEM image (**b**), HRTEM image (**c**), HAADF-STEM image (**d**), and elemental mapping images (**e**–**h**) of 0.37 wt% $Ni(OH)_2/ZnIn_2S_4$ composite.

Our results clearly demonstrate that the introduction of $Ni(OH)_2$ nanoflake during the synthesis does not significantly alert the formation dynamic of $ZnIn_2S_4$ nanosheets. Next, TEM and HRTEM measurements were applied to get further detailed structural information of 0.37 wt% $Ni(OH)_2/ZnIn_2S_4$ composite. As indicated (Figure 2b), a clear

ultra-thin-layered nanostructure was observed for $Ni(OH)_2/ZnIn_2S_4$ composite, which is in line with SEM results (Figure 2a). Further HRTEM investigation (Figure 2c) unambiguously shows the interfacial region of $ZnIn_2S_4$ and $Ni(OH)_2$, and as indicated, the lattice fringes with spacing at 0.27 and 0.32 nm could be ascribed to (110) plane of hexagonal $Ni(OH)_2$ and (102) plane of hexagonal $ZnIn_2S_4$, respectively [27–29]. No selected area electron diffraction (SEAD) signal of $Ni(OH)_2$ was observed for 0.37 wt% $Ni(OH)_2/ZnIn_2S_4$ composite compared with that of $Ni(OH)_2$ (Figure S3), which is assumed to be due to the low amount of $Ni(OH)_2$ in the composite. HAADF-STEM (Figure 2d) and the corresponding elemental mapping results (Figure 2e–h) revealed the homogeneous distribution of Zn, In, S, and Ni elements throughout the sample, strongly verifying the successful synthesis of the designed structure. EDX measurement (Figure S4) further verifies the existence of Ni, though its content is low.

To confirm the chemical state of different elements of the as-prepared samples, XPS measurements were further carried out. Figure 3a represents the XPS survey spectra of $ZnIn_2S_4$ and 0.37 wt% $Ni(OH)_2/ZnIn_2S_4$ composite, which confirms the existence of the designated elements only except for Ni. Furthermore, as shown in Figure 3b, Zn 2p XPS spectra of $ZnIn_2S_4$ and $Ni(OH)_2/ZnIn_2S_4$ composite exhibit two peaks at 1044.2 and 1021.1 eV, which correspond to Zn $2p_{1/2}$ and Zn $2p_{3/2}$ of $ZnIn_2S_4$, respectively, evidencing the existence of Zn^{2+} in the sample [30,31]. Peaks (Figure 3c) at 452.2 and 444.5 eV can be indexed to In $3d_{3/2}$ and In $3d_{5/2}$, confirming that element In in the sample is in the form of a trivalent cation [32]. In addition, the binding energies of S 2p peak (Figure 3d) were split into two peaks $2p_{1/2}$ at 162.4 and $2p_{3/2}$ at 161.1 eV, which was proved to be the S^{2-} typical characteristic in metal sulfides [33]. However, it should be mentioned here that no signal of Ni 2p was detected, which is considered to be due to the extremely low amount of $Ni(OH)_2$ in the sample.

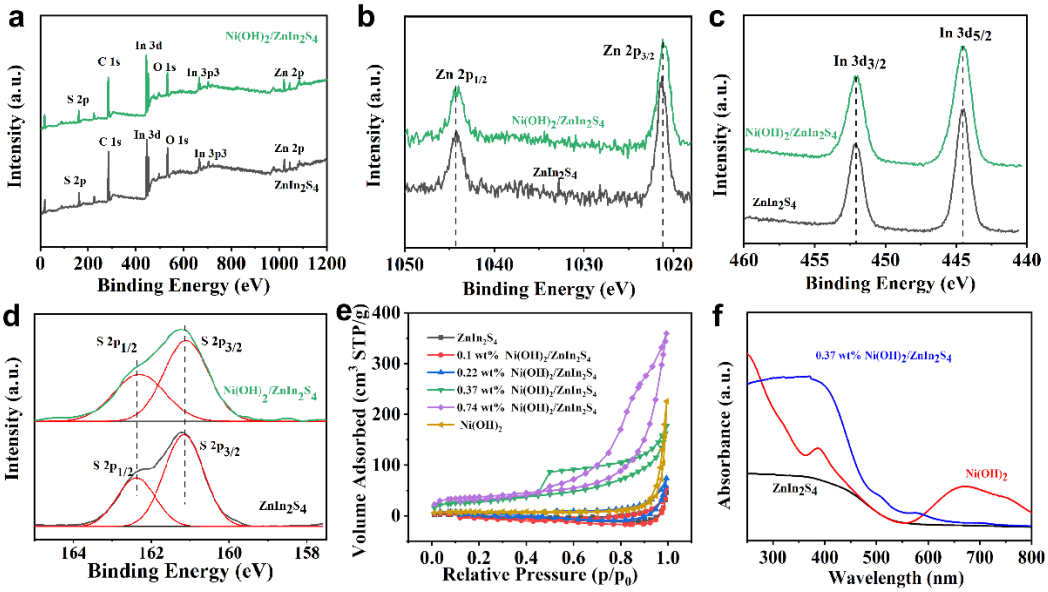

Figure 3. XPS survey spectra (**a**), Zn 2p (**b**), In 3d (**c**), and S 2p (**d**) of $ZnIn_2S_4$ and 0.37 wt% $Ni(OH)_2/ZnIn_2S_4$ composite, nitrogen adsorption–desorption isotherms (**e**) of different samples, UV–VIS diffuse reflectance spectra (**f**) of $ZnIn_2S_4$, $Ni(OH)_2$, and 0.37 wt% $Ni(OH)_2/ZnIn_2S_4$ composite samples.

BET measurements were then applied to evaluate the surface area of different samples. As indicated (Figure 3e and Table S2), with the increase in $Ni(OH)_2$ in the composite, the surface area is gradually increased from 0.51 m^2/g ($ZnIn_2S_4$) to 124.65 m^2/g (0.74 wt% $Ni(OH)_2/ZnIn_2S_4$), while the pore size seems not to follow that rule. In addition, all the samples exhibit type IV (Brunauer–Deming–Deming–Teller classification), and the

shape of the three hysteresis loops is type H3, assumed to be related to the aggregation of particles [16,34].

The absorbance properties of the as-obtained samples were then investigated by UV–VIS diffuse reflection spectroscopy. As shown (Figure 3f), the absorption of $Ni(OH)_2$ consists of two wide absorption bands at 390–500 nm and 600–800 nm, corresponding to the d-d transition of Ni [19,35]. On the other hand, for the composite samples, the absorption characteristic does not show an obvious difference with varying $Ni(OH)_2$ content in our case (Figure S5). In addition, new weak absorbance in the range of 600 to 800 nm, when compared with that of $ZnIn_2S_4$, further confirms the existence of $Ni(OH)_2$.

The H_2 photogeneration performance of different samples was evaluated by using TEOA as a sacrificial reagent under visible light illumination (>420 nm). Figure 4a shows the photocatalytic H_2 evolution versus illumination time of different samples. The results show that $Ni(OH)_2$ does not give any photocatalytic activity, while pure $ZnIn_2S_4$ only exhibits a pretty low activity (0.13 mL h^{-1}), which is assumed to be related to the fast recombination rate of charge carriers. Exceptionally, the 0.37 wt% $Ni(OH)_2/ZnIn_2S_4$ composite exhibits much higher activity for H_2 photogeneration, where obvious bubbles were observed after the reaction (Figure S6); however, the physical mixed control sample with the same content only shows moderate activity, which is only slightly higher than that of pure $ZnIn_2S_4$. Our results clearly demonstrate the importance of our strategy for obtaining the composite to achieve high performance of photocatalytic H_2 evolution. Further optimizing the amount of $Ni(OH)_2$ introduced in the composite reveals that content at 0.37 wt% gives the best performance of 0.52 mL h^{-1} (5 mg) (i.e., 4640 μmol h^{-1} g^{-1} (Figure 4b)), which is comparable with the recent benchmarking results (Table S3). The long-term stability test of 0.37 wt% $Ni(OH)_2/ZnIn_2S_4$ (Figure 4c) indicates good stability even after four cycles of photocatalytic reaction.

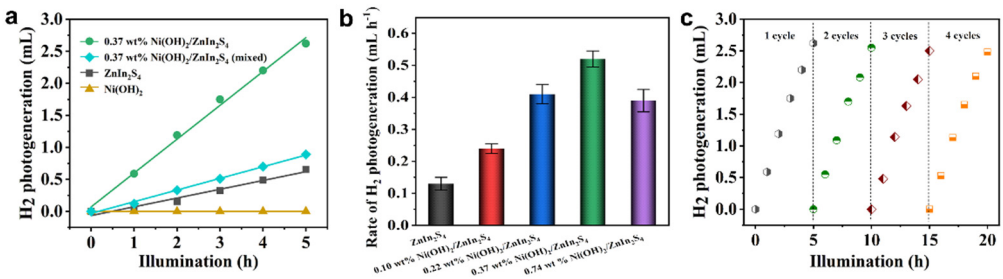

Figure 4. (**a**) H_2 evolution curves versus illumination time of visible light (λ > 420 nm) of $ZnIn_2S_4$, $Ni(OH)_2$, 0.37 wt%-$Ni(OH)_2/ZnIn_2S_4$, and 0.37 wt%-$Ni(OH)_2/ZnIn_2S_4$ (mixed). (**b**) H_2 evolution rate of $ZnIn_2S_4$, $Ni(OH)_2$, and $Ni(OH)_2/ZnIn_2S_4$ with different amounts of $Ni(OH)_2$ involved. The data were obtained from three individual experiments. (**c**) H_2 evolution stability test of 0.37 wt% $Ni(OH)_2/ZnIn_2S_4$ under the illumination of visible light (λ > 420 nm).

To elaborate on the underlying mechanism of this interesting activity enhancement, PL emission and lifetime spectra, time-resolved photocurrent, and electrochemical technique were employed. As indicated (Figure 5a), $ZnIn_2S_4$ exhibits a strong broadband PL emission in the range of 500–700 nm [36], while the obvious decrease in the PL intensity of samples after introducing $Ni(OH)_2$ is observed, and the corresponding degree is increased with the increase in the introduced amount of $Ni(OH)_2$, which is assumed to be attributed to the efficient photogenerated charge transfer from $ZnIn_2S_4$ to $Ni(OH)_2$, thus decreasing the probability of emission relaxation of carriers in $ZnIn_2S_4$. The process is expected to be beneficial to the charge separation in the composite, correlating with the enhancement of the photocatalytic activity of the catalyst [37,38]. In addition, time-resolved photocurrent spectra (Figure 5b) indicate that all the composite samples exhibit higher response than pure $ZnIn_2S_4$ or $Ni(OH)_2$, which strongly signifies the critical role of $Ni(OH)_2$ for efficient charge separation.

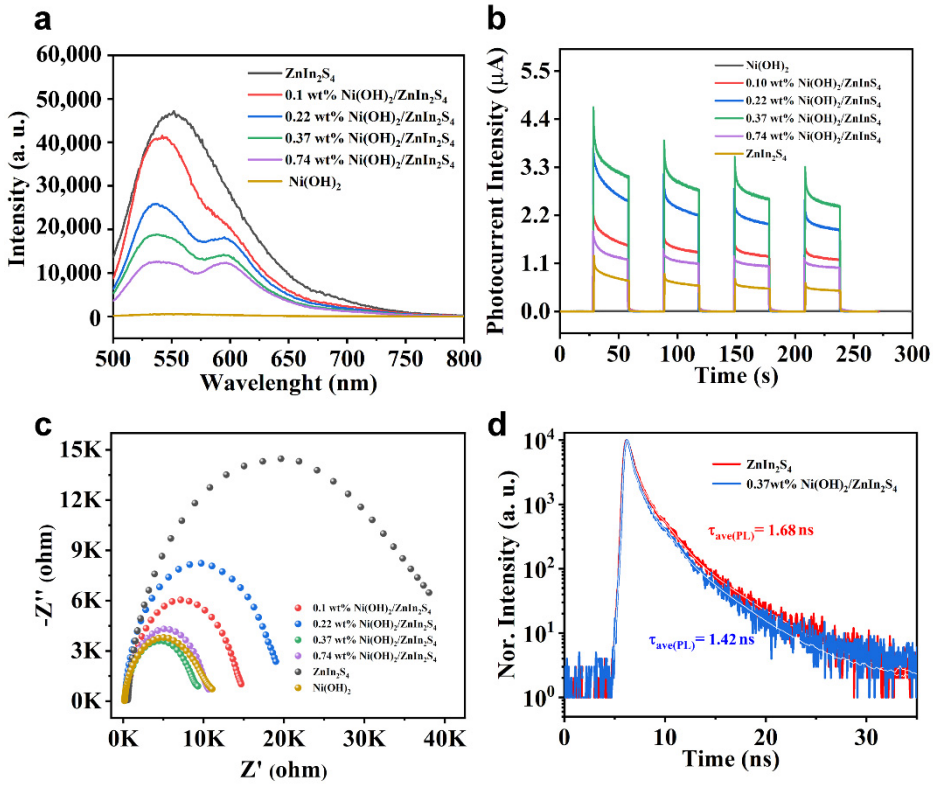

Figure 5. PL spectra (**a**) and transient photocurrent responses (**b**) of pure $ZnIn_2S_4$, $Ni(OH)_2$, and $Ni(OH)_2/ZnIn_2S_4$ composite samples with different amounts of $Ni(OH)_2$ involved. EIS (**c**) of different samples. PL lifetime decay curves (**d**) of $ZnIn_2S_4$ (red) and 0.37 wt% $Ni(OH)_2/ZnIn_2S_4$ (blue), respectively.

The charge transfer property of different samples was further evaluated by electrochemical impedance spectroscopy (EIS). As indicated (Figure 5c), the smallest Nyquist plot demonstrates its fast charge transfer property of 0.37 wt% $Ni(OH)_2/ZnIn_2S_4$ composite [39]. Further PL lifetime results (Figure 5d and Table S4) of $ZnIn_2S_4$ and 0.37 wt% $Ni(OH)_2/ZnIn_2S_4$ indicate that after the incorporation of the tiny amount of $Ni(OH)_2$ into $ZnIn_2S_4$, the relevant average lifetime ($\tau_{ave(PL)}$) is decreased from 1.68 to 1.42 ns, unambiguously revealing the charge accelerating role of $Ni(OH)_2$.

All of the above results intensely evidence that the boosting of the performance of the composite catalyst is highly possible, originated from the relatively high surface area and efficient charge carrier separation through the formation of the designed heterogeneous structure. Besides, it has been widely recognized that $Ni(OH)_2$ could act as the co-catalyst to accept the photoinduced electrons and further complete a subsequent proton reduction reaction during the photocatalytic hydrogen evolution process [40–42]. Therefore, based on all of these results, a probable mechanism for the $Ni(OH)_2/ZnIn_2S_4$ composite to boost the photocatalytic hydrogen evolution activity was proposed (Scheme 1). Under the illumination of visible light, the electron is excited from the valence band of $ZnIn_2S_4$ into the conduction band, followed by the subsequent quick transfer into $Ni(OH)_2$ to contribute to the proton reduction reaction. Since the position of the minimum conduction band of $ZnIn_2S_4$ is −1.35 V, which is more negative than the reduction potential of H^+/H_2 [43], the electron generated in $ZnIn_2S_4$ possesses the adequate ability to drive the proton reduction reaction. Meanwhile, the left hole would be consumed by TEOA, accompanied by the formation of the relevant oxidation products. Owing to the existence of $Ni(OH)_2$, the electron photoinduced in $ZnIn_2S_4$ is effectively inhibited, which results in the significant enhancement of the photocatalytic activity of the relevant composite.

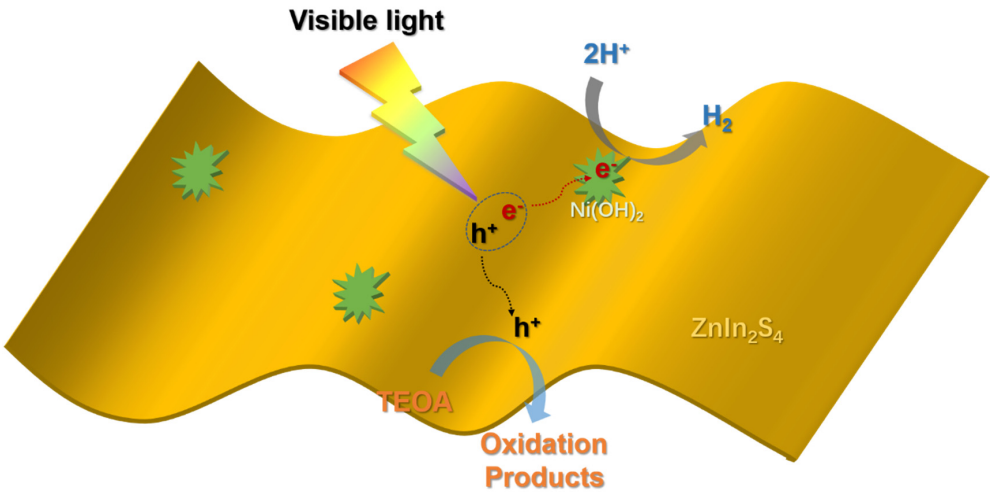

Scheme 1. Schematic illustration of the plausible underlying charge transfer mechanism of the hydrogen photogeneration process.

4. Conclusions

In this work, we designed and prepared a $Ni(OH)_2$-modified 2D $ZnIn_2S_4$ heterogeneous photocatalyst to achieve the high performance of photocatalytic H_2 evolution under visible light illumination. Benefiting its unique structure, under optimal conditions, the obtained sample exhibits superior activity for H_2 photogeneration. Furthermore, the plausible underlying mechanism is also proposed after the detailed investigations. It is hoped that our tactic and obtained information could provide useful information for the future design of a high-performance photocatalyst.

Supplementary Materials: The following supporting information can be downloaded at: https://www.mdpi.com/article/10.3390/nano12060946/s1: Table S1: The actual chemical compositions of the prepared samples; Table S2: BET surface area and pore size distribution of different samples; Table S3: Photocatalytic H_2 evolution results of some related works reported recently; Table S4: Detailed time-resolved transient PL decay fitting data of $ZnIn_2S_4$ and 0.37 wt% $Ni(OH)_2/ZnIn_2S_4$, respectively; Figure S1: XRD patterns of the samples after the preheating treatment before BET measurements; Figure S2: SEM image and enlarged SEM images of pure $Ni(OH)_2$ sheets (a,d), $ZnIn_2S_4$ (b,e) and 0.37 wt% $Ni(OH)_2/ZnIn_2S_4$ composite (c,f); Figure S3: SEAD images of $Ni(OH)_2$ (a), $ZnIn_2S_4$ (b), and 0.37 wt% $Ni(OH)_2/ZnIn_2S_4$ (c), respectively; Figure S4: EDX spectrum of the 0.37 wt% $Ni(OH)_2/ZnIn_2S_4$ composite; Figure S5: UV–VIS diffuse reflectance spectra of $Ni(OH)_2/ZnIn_2S_4$ composite samples with different amounts of $Ni(OH)_2$ introduced; Figure S6: Photograph of the photocatalytic reactor with 0.37 wt% $Ni(OH)_2/ZnIn_2S_4$ as photocatalyst during reaction.

Author Contributions: Conceptualization, H.W. and B.S.; methodology, H.W. and B.S.; validation, S.L. and C.W.; formal analysis, H.W. and B.S.; investigation, H.W. and X.Y.; writing—original draft preparation, H.W. and B.S.; writing—review and editing, H.W., B.S., Y.C. and X.Y.; visualization, B.L., H.L. and Y.L.; supervision, X.Y. All authors have read and agreed to the published version of the manuscript.

Funding: This research was funded by the science and technology development project of Jilin province, China (Nos. 20190201286JC and 20210203098SF), and financial support from Key Laboratory for Comprehensive Energy Saving of Cold Regions Architecture of the Ministry of Education.

Data Availability Statement: The data presented in this study are available on request from the corresponding author.

Conflicts of Interest: The authors declare no conflict of interest.

References

1. Nishiyama, H.; Yamada, T.; Nakabayashi, M.; Maehara, Y.; Yamaguchi, M.; Kuromiya, Y.; Nagatsuma, Y.; Tokudome, H.; Akiyama, S.; Watanabe, T.; et al. Photocatalytic solar hydrogen production from water on a 100 m^2 scale. *Nature* **2021**, *598*, 304–307. [CrossRef] [PubMed]
2. Takata, T.; Jiang, J.; Sakata, Y.; Nakabayashi, M.; Shibata, N.; Nandal, V.; Seki, K.; Hisatomi, T.; Domen, K. Photocatalytic water splitting with a quantum efficiency of almost unity. *Nature* **2020**, *581*, 411–414. [CrossRef] [PubMed]
3. Chen, L.; Gu, Q.; Hou, L.; Zhang, C.; Lu, Y.; Wang, X.; Long, J. Molecular p-n heterojunction-enhanced visible light hydrogen evolution over a N-doped TiO_2 photocatalyst. *Catal. Sci. Technol.* **2017**, *7*, 2039–2049. [CrossRef]
4. Bi, G.; Wen, J.; Li, X.; Liu, W.; Xie, J.; Fang, Y.; Zhang, W. Efficient visible-light photocatalytic H_2 evolution over metal-free g-C_3N_4 co-modified with robust acetylene black and $Ni(OH)_2$ as dual co-catalysts. *RSC Adv.* **2016**, *6*, 31497–31506. [CrossRef]
5. Shafi, A.; Ahmad, N.; Sultana, S.; Sabir, S.; Khan, M.Z. Ag_2S-Sensitized NiO-ZnO Heterostructures with Enhanced Visible Light Photocatalytic Activity and Acetone Sensing Property. *ACS Omega* **2019**, *4*, 12905–12918. [CrossRef] [PubMed]
6. Dang, H.; Dong, X.; Dong, Y.; Fan, H.; Qiu, Y. Enhancing the photocatalytic H_2 evolution activity of red phosphorous by using noble-metal-free $Ni(OH)_2$ under photoexcitation up to 700 nm. *RSC Adv.* **2014**, *4*, 44823–44826. [CrossRef]
7. Chen, Y.; Huang, R.; Chen, D.; Wang, Y.; Liu, W.; Li, X.; Li, Z. Exploring the Different Photocatalytic Performance for Dye Degradations over Hexagonal $ZnIn_2S_4$ Microspheres and Cubic $ZnIn_2S_4$ Nanoparticles. *ACS Appl. Mater. Interfaces* **2012**, *4*, 2273–2279. [CrossRef]
8. Pan, Y.; Yuan, X.; Jiang, L.; Yu, H.; Zhang, J.; Wang, H.; Guan, R.; Zeng, G. Recent advances in synthesis, modification and photocatalytic applications of micro/nano-structured zinc indium sulfide. *Chem. Eng. J.* **2018**, *354*, 407–431. [CrossRef]
9. Wang, J.; Sun, S.; Zhou, R.; Li, Y.; He, Z.; Ding, H.; Chen, D.; Ao, W. A review: Synthesis, modification and photocatalytic applications of $ZnIn_2S_4$. *J. Mater. Sci. Technol.* **2021**, *78*, 1–19. [CrossRef]
10. Li, Y.; Zhang, K.; Peng, S.; Lu, G.; Li, S. Photocatalytic hydrogen generation in the presence of ethanolamines over Pt/$ZnIn_2S_4$ under visible light irradiation. *J. Mol. Catal. A Chem.* **2012**, *363*, 354–361. [CrossRef]
11. Yang, W.; Zhang, L.; Xie, J.; Zhang, X.; Liu, Q.; Yao, T.; Wei, S.; Zhang, Q.; Xie, Y. Enhanced photoexcited carrier separation in oxygen-doped $ZnIn_2S_4$ nanosheets for hydrogen E volution. *Angew. Chem. Int. Ed.* **2016**, *55*, 6716–6720. [CrossRef] [PubMed]
12. Guo, X.; Peng, Y.; Liu, G.; Xie, G.; Guo, Y.; Zhang, Y.; Yu, J. An Efficient $ZnIn_2S_4$@$CuInS_2$ Core−Shell p−n Heterojunction to Boost Visible-Light Photocatalytic Hydrogen Evolution. *J. Phys. Chem. C* **2020**, *124*, 5934–5943. [CrossRef]
13. Yang, R.; Song, K.; He, J.; Fan, Y.; Zhu, R. Photocatalytic Hydrogen Production by RGO/$ZnIn_2S_4$ under Visible Light with Simultaneous Organic Amine Degradation. *ACS Omega* **2019**, *4*, 11135–11140. [CrossRef] [PubMed]
14. Lu, X.; Xie, J.; Liu, S.; Adamski, A.; Chen, X.; Li, X. Low-Cost Ni_3B/$Ni(OH)_2$ as an Ecofriendly Hybrid Cocatalyst for Remarkably Boosting Photocatalytic H_2 Production over g C_3N_4 Nanosheets. *ACS Sustain. Chem. Eng.* **2018**, *6*, 13140–13150. [CrossRef]
15. Yang, L.; Zhu, Y.; Tong, H.; Liang, Z.; Wang, W. Hierarchical -$Ni(OH)_2$ and NiO Carnations Assembled from Nanosheet Building Blocks. *Cryst. Growth Des.* **2007**, *7*, 2716–2719. [CrossRef]
16. Jia, D.; Gao, H.; Dong, W.; Fan, S.; Dang, R.; Wang, G. Hierarchical α $Ni(OH)_2$ Composed of Ultrathin Nanosheets with Controlled Interlayer Distances and Their Enhanced Catalytic Performance. *ACS Appl. Mater. Interfaces* **2017**, *9*, 20476–20483. [CrossRef] [PubMed]
17. Ong, W.L.; Ng, S.W.L.; Zhang, C.; Hong, M.; Ho, G.W. 2D hydrated layered $Ni(OH)_2$ structure with hollow TiO_2 nanocomposite directed chromogenic and catalysis capabilities. *J. Mater. Chem. A* **2016**, *4*, 13307–13315. [CrossRef]
18. Vamvasakis, I.; Papadas, I.T.; Tzanoudakis, T.; Drivas, C.; Choulis, S.A.; Kennou, S.; Armatas, G.S. Visible-Light Photocatalytic H_2 Production Activity of β $Ni(OH)_2$ Modified CdS Mesoporous Nanoheterojunction Networks. *ACS Catal.* **2018**, *8*, 8726–8738. [CrossRef]
19. Yu, J.; Wang, S.; Cheng, B.; Lin, Z.; Huang, F. Noble metal-free $Ni(OH)_2$–g-C_3N_4 composite photocatalyst with enhanced visible-light photocatalytic H_2-production activity. *Catal. Sci. Technol.* **2013**, *3*, 1782–1789. [CrossRef]
20. Li, X.; Wang, X.; Zhu, J.; Li, Y.; Zhao, J.; Li, F. Fabrication of two-dimensional Ni_2P/$ZnIn_2S_4$ heterostructures for enhanced photocatalytic hydrogen evolution. *Chem. Eng. J.* **2018**, *353*, 15–24. [CrossRef]
21. Yuan, Y.; Chen, D.; Zhong, J.; Yang, L.; Wang, J.; Liu, M.; Tu, W.; Yu, Z.; Zou, Z. Interface engineering of a noble-metal-free 2D-2D MoS_2/Cu-$ZnIn_2S_4$ photocatalyst for enhanced photocatalytic H2 production. *J. Mater. Chem. A* **2017**, *5*, 15771–15779. [CrossRef]
22. Guo, Z.; Hou, H.; Zhang, J.; Cai, P.; Lin, J. Prominent roles of $Ni(OH)_2$ deposited on $ZnIn_2S_4$ microspheres in efficient charge separation and photocatalytic H_2 evolution. *RSC Adv.* **2021**, *11*, 12442–12448. [CrossRef]
23. Nagappagari, L.R.; Samanta, S.; Sharma, N.; Battula, V.R.; Kailasam, K. Synergistic effect of a noble metal free $Ni(OH)_2$ co-catalyst and a ternary $ZnIn_2S_4$/g-C_3N_4 heterojunction for enhanced visible light photocatalytic hydrogen evolution. *Sustain. Energy Fuels* **2020**, *4*, 750–759. [CrossRef]
24. Gao, M.; Sheng, W.; Zhuang, Z.; Fang, Q.; Gu, S.; Jiang, J.; Yan, Y. Efficient Water Oxidation Using Nanostructured α Nickel-Hydroxide as an Electrocatalyst. *J. Am. Chem. Soc.* **2014**, *136*, 7077–7084. [CrossRef]
25. Xu, L.; Ding, Y.; Chen, C.; Zhao, L.; Rimkus, C.; Joesten, R.; Sui, S. 3D Flowerlike α-Nickel Hydroxide with Enhanced Electrochemical Activity Synthesized by Microwave-Assisted Hydrothermal Method. *Chem. Mater.* **2008**, *20*, 308–316. [CrossRef]
26. Peng, X.; Ye, L.; Ding, Y.; Yi, L.; Zhang, C.; Wen, Z. Nanohybrid photocatalysts with $ZnIn_2S_4$ nanosheets encapsulated UiO-66 octahedral nanoparticles for visible-light-driven hydrogen generation. *Appl. Catal. B Environ.* **2020**, *260*, 118152. [CrossRef]

27. Zhang, S.; Liu, X.; Liu, C.; Luo, S.; Wang, L.; Cai, T.; Zeng, Y.; Yuan, J.; Dong, W.; Pei, Y.; et al. MoS_2 quantum dot growth induced by S vacancies in a $ZnIn_2S_4$ monolayer: Atomic-level heterostructure for photocatalytic hydrogen production. *ACS Nano.* **2018**, *12*, 751–758. [CrossRef]
28. Zhao, J.; Yan, X.; Zhao, N.; Li, X.; Lu, B.; Zhang, X.; Yu, H. Cocatalyst designing: A binary noble-metal-free cocatalyst system consisting of $ZnIn_2S_4$ and $In(OH)_3$ for efficient visible-light photocatalytic water splitting. *RSC Adv.* **2018**, *8*, 4979–4986. [CrossRef]
29. Wang, S.; Guan, B.; Wang, X.; Lou, X. Formation of hierarchical Co_9S_8@$ZnIn_2S_4$ heterostructured cages as an efficient photocatalyst for hydrogen evolution. *J. Am. Chem. Soc.* **2018**, *140*, 15145–15148. [CrossRef]
30. Liu, Y.; Li, C.; Li, X.; Yu, W.B.; Dong, W.D.; Zhao, H.; Hu, Z.Y.; Deng, Z.; Wang, C.; Wu, S.J. Molybdenum Disulfide Quantum Dots Directing Zinc Indium Sulfide Heterostructures for Enhanced Visible Light Hydrogen Production. *J. Colloid Interface Sci.* **2019**, *551*, 111–118. [CrossRef]
31. Liu, Q.; Wang, M.; He, Y.; Wang, X.; Su, W. Photochemical Route for Synthesizing Co-P Alloy Decorated $ZnIn_2S_4$ with Enhanced Photocatalytic H_2 Production Activity under Visible Light Irradiation. *Nanoscale* **2018**, *10*, 19100–19106. [CrossRef] [PubMed]
32. Ye, L.; Wen, Z. $ZnIn_2S_4$ nanosheets decorating WO_3 nanorods core-shell hybrids for boosting visible-light photocatalysis hydrogen generation. *Int. J. Hydrog. Energy* **2019**, *44*, 3751–3759. [CrossRef]
33. Huang, L.; Han, B.; Huang, X.; Liang, S.; Deng, Z.; Chen, W.; Peng, M.; Deng, H. Ultrathin 2D/2D $ZnIn_2S_4/MoS_2$ Hybrids for Boosted Photocatalytic Hydrogen Evolution under Visible Light. *J. Alloys Compd.* **2019**, *798*, 553–559. [CrossRef]
34. Zhang, L.; Wang, G.; Jin, Z. Growth of $Zn_{0.5}Cd_{0.5}S$/a-$Ni(OH)_2$ heterojunction by a facile hydrothermal transformation efficiently boosting photocatalytic hydrogen production. *New J. Chem.* **2019**, *43*, 6411–6421. [CrossRef]
35. Ran, J.; Yu, J.; Jaroniec, M. Ni(OH)2 modified CdS nanorods for highly efficient visible-light-driven photocatalytic H2 generation. *Green Chem.* **2011**, *13*, 2708–2713. [CrossRef]
36. Yang, M.; Xu, Y.; Lu, W.; Zeng, K.; Zhu, H.; Xu, Q.; Ho, G. Self-surface charge exfoliation and electrostatically coordinated 2D hetero-layered hybrids. *Nat. Commun.* **2017**, *8*, 14224–14232. [CrossRef]
37. Yan, A.; Shi, X.; Huang, F.; Fujitsuka, M.; Majima, T. Efficient photocatalytic H_2 evolution using $NiS/ZnIn_2S_4$ heterostructures with enhanced charge separation and interfacial charge transfer. *Appl. Catal. B Environ.* **2019**, *250*, 163–170. [CrossRef]
38. Geng, M.; Peng, Y.; Zhang, Y.; Guo, X.; Yu, F.; Yang, X.; Xie, G.; Dong, W.; Liu, C.; Li, J.; et al. Hierarchical $ZnIn_2S_4$: A promising cocatalyst to boost visible-light-driven photocatalytic hydrogen evolution of $In(OH)_3$. *Int. J. Hydrog. Energy* **2019**, *44*, 5787–5798. [CrossRef]
39. Zeng, H.; Li, Z.; Li, G.; Cui, X.; Jin, M.; Xie, T.; Liu, L.; Jiang, M.; Zhong, X.; Zhang, Y.; et al. Interfacial Engineering of TiO_2/Ti_3C_2 MXene/Carbon Nitride Hybrids Boosting Charge Transfer for Efficient Photocatalytic Hydrogen Evolution. *Adv. Energy Mater.* **2021**, *12*, 2102765. [CrossRef]
40. Ran, J.; Zhang, J.; Yu, J.; Qiao, S.Z. Enhanced Visible-Light Photocatalytic H_2 Production by $Zn_xCd_{1-x}S$ Modiied with Earth-Abundant Nickel-Based Cocatalysts. *ChemSusChem* **2014**, *7*, 3426–3434. [CrossRef]
41. Gao, R.; Xiong, L.; Huang, L.; Chen, W.; Li, X.; Liu, X.; Mao, L. A new structure of Pt NF@$Ni(OH)_2$/CdS heterojunction: Preparation, characterization and properties in photocatalytic hydrogen generation. *Chem. Eng. J.* **2022**, *430*, 132726. [CrossRef]
42. Yan, Z.; Yu, X.; Zhang, Y.; Jia, H.; Sun, Z.; Du, P. Enhanced visible light-driven hydrogen production from water by a noble-metal-free system containing organic dye-sensitized titanium dioxide loaded with nickel hydroxide as the cocatalyst. *Appl. Catal. B Environ.* **2014**, *160*, 173–178. [CrossRef]
43. Chen, W.; Liu, T.; Huang, T.; Liu, X.; Yang, X. Novel mesoporous P-doped graphitic carbon nitride nanosheets coupled with $ZnIn_2S_4$ nanosheets as efficient visible light driven heterostructures with remarkably enhanced photo-reduction activity. *Nanoscale* **2016**, *8*, 3711–3719. [CrossRef] [PubMed]